JOURNAL OF GEOPHYSICAL RESEARCH, VOL. 85, NO. C7, PAGES 3964–3970, JULY 20, 1980

Optical Determination of the Phase Velocity of Short Gravity Waves

B. L. GOTWOLS AND G. B. IRANI

The Johns Hopkins University, Applied Physics Laboratory, Laurel, Maryland 20810

Images of short wind-driven gravity waves were taken from an offshore platform, using a charge coupled device television camera recording diffuse sky radiance reflected from the ocean surface. A two-dimensional power spectrum was calculated from nine statistically independent images. The resultant ensemble-averaged spectrum exhibited good statistical stability and provided information on the angular spread and direction of the wave components present. One-dimensional sampling of each image in a sequence allowed a space-time image to be constructed which clearly shows the effects of wave dispersion as well as the modulation of the phase velocities of the short wavelength waves by the long wavelength components. An ensemble-averaged space-time spectrum, when combined with the directional parameters, is compared with the predictions of linear gravity wave dispersion theory. Two distinct wave systems were present: the local wind driven system showed a space-time spectrum in agreement with linear theory out to ~1 cyc/m, but with excess phase velocity at higher spatial frequencies. The second wave system, which was presumably generated by a distant wind field, showed a deficiency in phase velocity when compared to linear theory.

INTRODUCTION

Wave-tank measurements of wind-driven gravity waves by *Ramamonjiarisoa and Coantic* [1976], *Lake and Yuen* [1978], and *Rikiishi* [1978], have indicated that the propagation of spectral components with spatial frequencies greater than the spatial frequency of the dominant wave is largely nondispersive. Above the dominant wave frequency the phase velocity was practically constant, in conflict with the prediction of linear theory. This finding is not confirmed, however, by *Plant and Wright* [1979] who find good agreement with linear wave theory after account is taken of advection by the wind drift current.

Ocean measurements of gravity waves are similarly mixed with regard to their phase velocity characteristics. *Von Zweck* [1970] examined two data sets and found that in one the phase velocity was in good agreement with linear theory and that in the other, at frequencies well above the frequency of the dominant wave, there was a slight excess in phase velocity (~10%). *Yefimov et al.* [1972] found excess phase velocity after averaging over a series of nine measurements. *Ramamonjiarisoa and Giovanangeli* [1978] reported one case where there was a significant deviation from linear theory and one case where there was good agreement.

In this paper we use the video recording of diffuse skylight reflected from the ocean surface as a means of remotely sensing one component of wave slope over an extremely large grid of points. This is an extension to the time domain of a technique for obtaining wave-slope directional spectra that was first demonstrated qualitatively by *Barber* [1949], and formalized by *Stilwell* [1969], *Stilwell and Pilon* [1974], *Kasevich* [1975], and others. The objective of the current paper is limited to demonstrating the feasibility of our technique for remotely measuring phase velocity. Since we have currently analyzed the data from only a single observing session, it will be left to later papers to explore the sensitivity of the propagation characteristics to environmental conditions.

Paper number 80C0302.
0148-0227/80/080C-0302$01.00

DESCRIPTION OF THE EXPERIMENT

Observations were made in September 1978 from the Stage I tower, which is operated by the Naval Coastal Systems Center, located in the Gulf of Mexico 19 km south of Panama City, Florida, in 30 m of water. Wind-wave images were obtained with a resolution of 240 pixels along field by 320 pixels across field using an RCA TC1160 BE charge coupled device (CCD) video camera. Two important advantages of a CCD sensor are that the transfer function from image radiance to output signal is linear over a wide range, and the temporal response is not affected by the partial image retention which is characteristic of conventional video sensors. Two steps were taken to improve the quantitative response of this commercially available camera. First, all of the camera's analog electronics were replaced with circuitry designed to be linear over the entire irradiance range of the CCD chip and to provide a smooth roll off at high frequency. (The unmodified camera has special edge enhancement circuitry, which is undesirable in our application.) Second, a synchronous rotating shutter was placed in front of the lens to eliminate the crosstalk between pixels which normally occurs in this frame transfer-type of CCD sensor owing to the image being present on the chip during electronic readout. The images were recorded on a video tape recorder at the standard television rate of 30 frames/s.

The wave images discussed in this paper were acquired in horizontal polarization at a depression angle of 30°, at a focal length of 38 mm, and with a Kodak 25A (red) filter to minimize contamination from upwelling radiation. The camera was located 25 m above the water. Hence, the field of measurement was a trapezoid with central dimensions of approximately 25 m along the field direction by 13 m across the field (see Figure 1).

Other instrumentation pertinent to this paper consisted of a two-axis current meter located at a depth of 3 m, an anemometer and direction vane at an altitude of 28 m, and a skyward-looking video camera equipped with a wide angle lens which allowed periodic recording of the sky radiance. A 15 element capacitive wave gauge array was also operated simul-

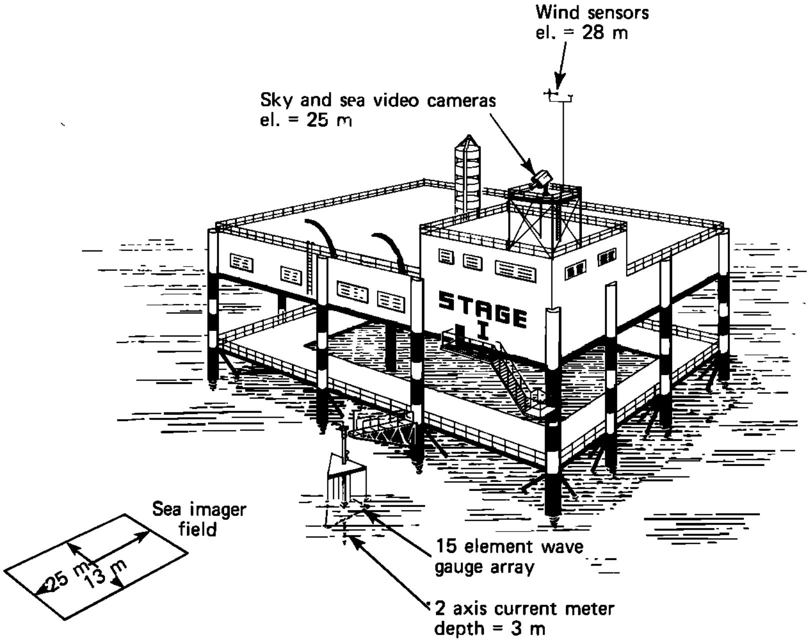

Fig. 1. Wave, current, and wind sensors deployed at the Stage I tower for the results reported.

taneously with the optical observations, but the results from only a single array element are currently available.

SPACE-TIME SPECTRUM

The description of our analysis technique begins with the three-dimensional power spectral density of a surface slope component. We shall assume throughout this paper that the surface slope component along the field of measurement is proportional to the radiant energy we actually measure. For brevity, the word 'spectrum' will be taken to mean surface slope component spectrum. Thus for small amplitude waves obeying the linear, deepwater, gravity dispersion relation, we have

$$G(\omega, k_x, k_y) = \tfrac{1}{2}F(k_x, k_y)\delta[\omega - (gk)^{1/2}] + \tfrac{1}{2}F(-k_x, -k_y)\delta[\omega + (gk)^{1/2}] \qquad (1)$$

where $G(\omega, k_x, k_y)$ is the (three-dimensional) wavenumber frequency spectrum, $k = (k_x^2 + k_y^2)^{1/2}$, and $F(k_x, k_y)$ is the (two-dimensional) wavenumber spectrum. The second term in (1) is entirely redundant to the first term; it applies only to negative (temporal) frequency and ensures that $G(-\omega, -k_x, -k_y) = G(\omega, k_x, k_y)$.

Before proceeding it will be helpful to point out that $F(k_x, k_y)$ is not the usual slope spectrum that is determined from wave images. Denoting this latter spectrum by $H(k_x, k_y)$, its relation to the above spectrum is

$$H(k_x, k_y) = \int_{-\infty}^{+\infty} G(\omega, k_x, k_y)\, d\omega = \tfrac{1}{2}F(k_x, k_y) + \tfrac{1}{2}F(-k_x, -k_y) \qquad (2)$$

$H(k_x, k_y)$ thus shows the familiar symmetry through the origin, whereas $F(k_x, k_y)$ generally does not. $F(k_x, k_y)$ separately encodes the wave propagation directions present in $G(\omega, k_x, k_y)$, whereas in $H(k_x, k_y)$ this directional information is lost. (This is sometimes called directional aliasing.)

Estimation of $G(\omega, k_x, k_y)$ from a temporal sequence of our images involves a staggering number of computations which we have reserved for a future paper. Our present results have been realized through a shortcut. The shortcut is to analyze the wave image radiance along a single line (the y axis) which is approximately parallel to the direction of propagation of the dominant wave. Thus our measurement of slope $s(x_0, y, t)$ could be used to calculate the autocovariance

$$R_s(Y, \tau) = \langle s(x_0, y, t)s(x_0, y + Y, t + \tau)\rangle \qquad (3)$$

The Fourier transform of this we shall call $S(\omega, k_y)$. In practice we used fast Fourier transform techniques to estimate $S(\omega, k_y)$. $S(\omega, k_y)$ is related to $G(\omega, k_x, k_y)$ through the relation

$$S(\omega, k_y) = \int_{-\infty}^{+\infty} G(\omega, k_x, k_y)\, dk_x \qquad (4)$$

Now assume a very narrow angular distribution of waves propagating in the positive x direction at an angle θ from the y axis. Thus

$$F(k_x, k_y) = \begin{cases} f[(k_x^2 + k_y^2)^{1/2}]\delta(k_x - k_y \tan\theta) & k_y \geq 0 \\ = 0 & k_y < 0 \end{cases} \qquad (5)$$

Substituting (5) into (1) and (4), and evaluating the integral, yields

$$S(\omega, k_y) = f(k_0)\delta[\omega - (gk_0)^{1/2}] \qquad (6)$$

where

$$k_0 = [k_y^2(1 + \tan^2\theta)]^{1/2} = \left|\frac{k_y}{\cos\theta}\right| \qquad (7)$$

and we have used the symmetry condition $S(-\omega, -k_y) = S(\omega, k_y)$ to express this result in terms of positive ω. Examining the argument of the delta function shows that our $S(\omega, k_y)$ has an associated dispersion relationship given by

$$\omega = (g\,|k_y/\cos\theta|)^{1/2} \qquad (8)$$

This could have been derived more easily by noting that $k_y = k\cos\theta$, solving for k, and substituting into the linear dispersion relation. However, the discussion above allowed us to introduce the various spectra with which we will be dealing.

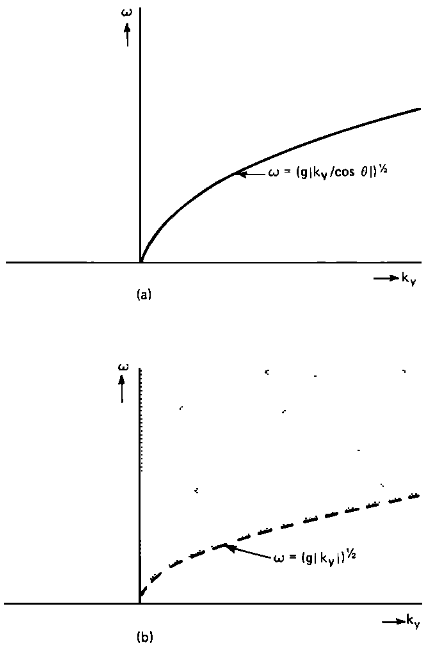

Fig. 2. Locus of nonzero values of $S(\omega, k_y)$ for waves with a velocity component in the $+y$ direction; (*a*) narrow angular spectrum oriented at angle θ to the y axis; (*b*) angularly 'isotropic' spectrum within the range $-90° \leq \theta \leq +90°$.

In Figure 2*a* we show a schematic sketch of the locus of nonzero values of $S(\omega, k_y)$ for this case of a narrow angular spectrum. If the spectrum instead consists of waves with wave vectors distributed over the range $-90° \leq \theta \leq 90°$, we see that $S(\omega, k_y)$ would fill the region shown in Figure 2*b*. The actual situation should be somewhere between these two extremes, with the center of the pattern governed by the mean direction of the waves.

The presence of a current **u** causes the dispersion relationship to include an additional term $\mathbf{u} \cdot \mathbf{k}$. We must again account for the direction of our spatial sampling baseline; consequently, the effective dispersion relation becomes

$$\omega = (g|k_y/\cos\theta|)^{1/2} + u|k_y/\cos\theta|\cos\alpha$$

where α is the angle between the current vector and the wave vector.

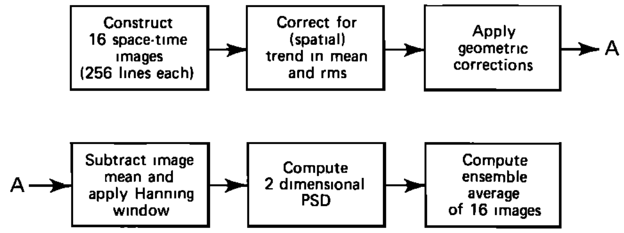

Fig. 4. Block diagram of the data reduction steps leading to the calculation of $S(\omega, k_y)$.

DATA REDUCTION

The space-time data from which $S(\omega, k_y)$ was calculated were assembled by digitizing a single line along the projected field of measurement from each of a sequence of 4096 images, corresponding to about 136.5 s. These data are broken into a subset of 16 space-time images, each consisting of 256 lines of data. Ultimately, a two-dimensional power spectrum was calculated for each of these space-time images.

The data were preconditioned to remove significant trends owing to variation of the Fresnel reflection coefficient with in-

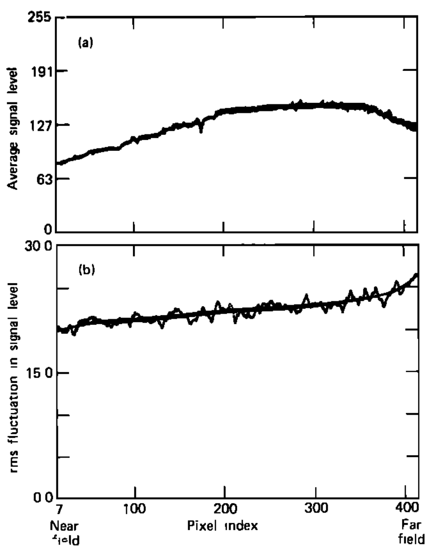

Fig. 3. (*a*) Average signal levels derived from one-dimensional sampling of 4096 images; (*b*) rms fluctuation in signal levels from the same data. The smooth curve is a least squares third-degree Chebyshev polynomial fit.

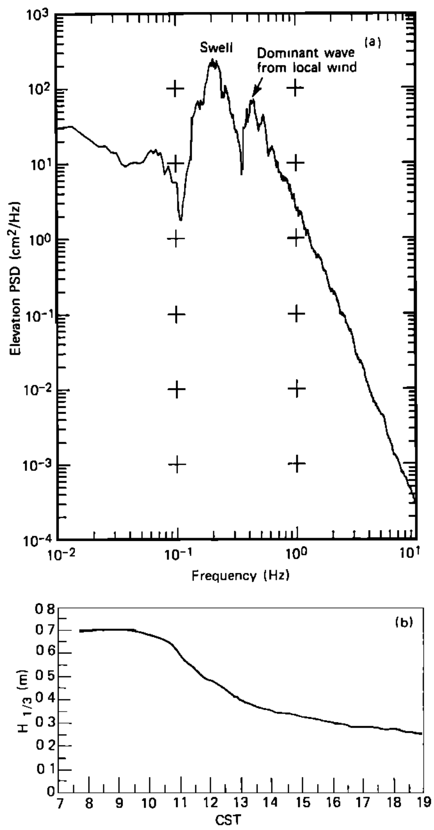

Fig. 5. (*a*) Sea surface elevation power spectral density (PSD) for an 11-min period centered on the time of the optical observations reported in this paper (1604 CST); (*b*) temporal evolution of significant wave height on the day of the optical observations.

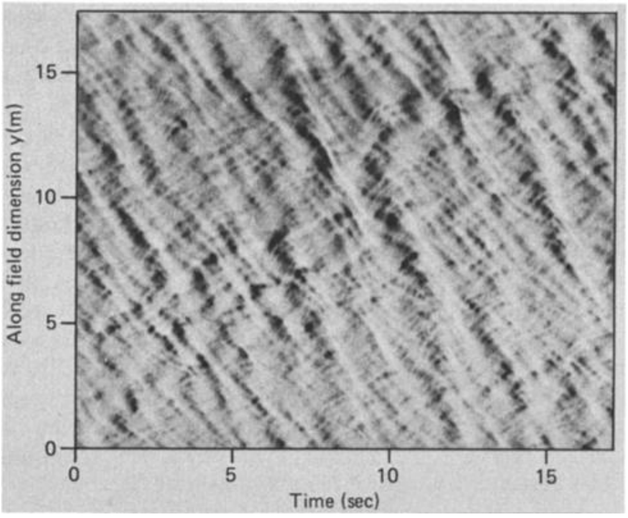

Fig. 6. Space-time image (1604 CST, September 27, 1978) which has been corrected for nonuniform brightness and geometric foreshortening (see text). Two wave systems are present: The stronger system appears as modulations sloping from upper left to lower right and clearly shows evidence of wave dispersion as well as modulation of the phase velocity of the short waves by the orbital velocity of the longer waves.

cidence angle, nonuniform camera response, and nonuniform sky radiance. At each of the pixels, both the average and the rms signal levels were calculated from the sequence of 4096 lines of data. Figure 3 shows the results of these computations. In Figure 3*a* the average signal level shows an increase with pixel index over the left half of the figure, followed by a flattening, and finally, a decline at the right edge of the figure. Since the angle of incidence and Fresnel reflection coefficient increase monotonically toward the far field (higher pixel index), it might be anticipated that this curve should increase monotonically with pixel index. We believe the nonmonotonic behavior is due to a nonuniform bias in the CCD sensor. Tests have shown that the fine scale structure present in Figure 3*a* is caused by irregularities in the CCD sensor and is not predominantly a residual owing to the individual wave images. Consequently, rather than smooth the average signal level by fitting a polynomial, we simply subtracted the mean levels from each of the 4096 lines in the data base.

The monotonic increase in rms fluctuation in signal level is readily apparent from the data in Figure 3*b*. A least squares third-degree Chebyshev polynomial fit to these rms values is shown as the smooth curve. This smoothed curve was normalized to unity at the center pixel index and was divided into each of the lines of the data base. This step effectively removes the 'gain change' that occurs along the field of measurement, predominantly as a result of the change in the Fresnel reflection coefficient with angle of incidence.

Owing to the shallow depression angle, there is significant foreshortening which causes a monochromatic wave on the ocean surface to appear to have a shorter wavelength in the far field than in the near field. This geometric distortion was eliminated by resampling each line of data (using linear interpolation) into an array of 256 points which were linearly spaced on the mean ocean surface. This was effectively a decimation of data points, but tests showed that there was not sufficient fine spatial structure in the original data for this to cause significant aliasing over the spatial frequency range analyzed in this paper.

The last two steps in preconditioning the data were to sub-

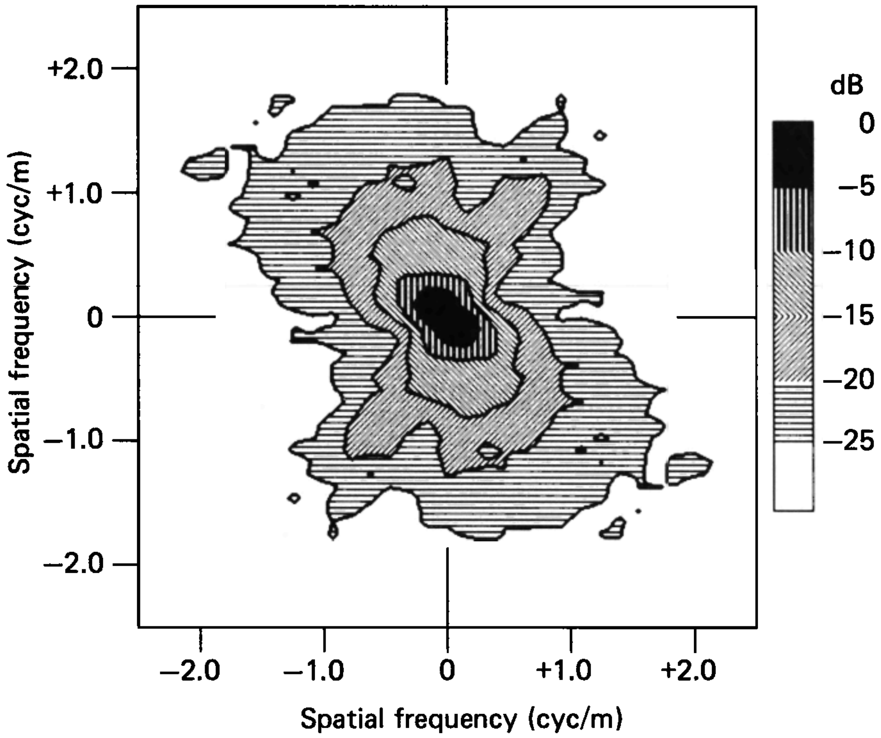

Fig. 7. Ensemble average of nine wave directional spectra calculated from a 256 by 256 point subset of the 480 by 512 point digitized CCD images. The images were separated in time by 17 s. The (normalized) spectral density has been compressed logarithmically and is encoded as five distinct levels, each separated by 5 dB. The figure is white where the level is more than 25 dB below the spectral maximum. The direction of the camera azimuth is parallel to the vertical axis.

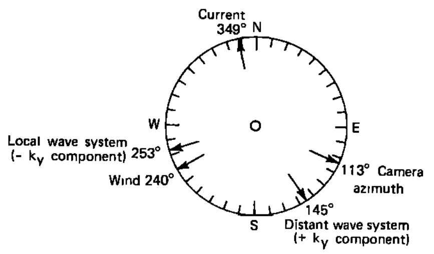

Fig. 8. Various azimuths relevant to the observations at 1604 CST on September 27, 1978. The wind and the current azimuths are drawn along the direction of the velocity vectors (contrary to the usual wind convention).

tract the average image value from each pixel and to multiply each of the 256 by 256 point space-time images by a two-dimensional Hanning window. A two-dimensional fast Fourier transform was calculated for each of the 16 images, and, after conversion to power spectral density, the results were averaged together. These steps are summarized schematically in Figure 4.

RESULTS

Before describing the results of our optical observations, it is useful to characterize the prevailing wind and wave conditions as measured in a more direct way. The wave elevation spectrum derived from a single element of our wave gauge array (see Figure 5*a*) exhibits a swell peak at 0.25 Hz and a dominant wind-driven wave frequency of 0.4 Hz. Using linear dispersion theory, we estimate that the wavelength of the dominant wave was approximately 9.8 m. This is somewhat shorter than the 16-m baseline of the observations we analyzed; hence the dominant wave number was resolved in the results which follow, whereas the swell peak was not. The significant wave height declined for 6 hours preceding the observations (Figure 5*b*). Similarly, the wind speed showed a gradual decline from 10 m/s at 0800 to 0.9 m/s at 1604 when the observations were made. The wind direction slowly varied during the day, generally coming out of the northeast and east. At the time of the observations, the wind vector azimuth (the direction in which the wind is traveling) was 240°.

A space-time image on which all preprocessing steps have been applied (except Hanning windowing) is shown in Figure 6. The predominant pattern runs from upper left to lower right and is due to gravity waves excited by the local wind field. There is a secondary pattern of much lower contrast which moves up and to the right. This pattern is caused by a second, much weaker wave system which is propagating in nearly the opposite direction to the local wind waves, and is presumably owing to a distant wind field.

In Figure 6 the wave velocity is proportional to slope. The influence of wave dispersion is immediately evident when it is noticed that the longer wavelength components have a steeper slope and therefore higher velocity, than the short wavelength components. This is qualitatively in agreement with conventional linear theory and suggests that the power spectral analysis which follows will not find a result in agreement with several of the published wave-tank measurements which suggest that the shorter wavelength waves propagate at a speed (independent of frequency) slightly less than that of the dominant

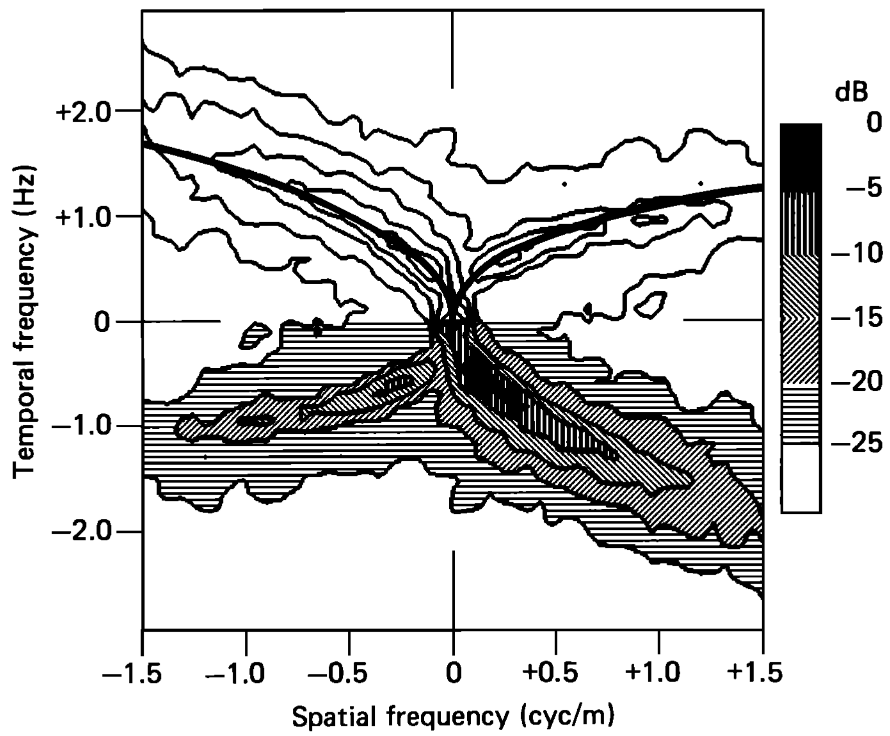

Fig. 9. Ensemble average of 16 space-time spectra from 1604–1606.3 CST on September 27, 1978. The (normalized) spectral density is encoded as five distinct levels, each separated by 5 dB. The figure is white where the level is more than 25 dB below the spectral maximum. (For clarity, shading has been omitted in the top half of the figure.) At spatial frequencies more negative than −1 cyc/m the wind-driven waves exhibit a spectrum which lies above the linear theory curve (heavy black line). Waves generated at some distance produce a spectrum at positive spatial frequencies which lies slightly below the prediction of linear theory.

wave. An interesting feature in Figure 6 is the obvious 'wiggly' nature of the short wavelength components when they cross a long wavelength component. This modulation of the short wavelength phase velocities is caused by the orbital current of the long wavelength waves. This effect will tend to smear the power spectral density over a band of space-time frequencies.

As was discussed earlier, to compare the space-time spectrum with theory it is necessary to know the average angle of propagation of the wave system with respect to the sampling baseline as well as the current magnitude and direction. The average current vector was obtained from the two-axis current meter mentioned earlier. The directions of the two wave systems were obtained by digitizing nine two-dimensional images and calculating an ensemble-average two-dimensional power spectrum. Geometric corrections were not applied to these images, so care had to be taken in assigning spatial frequency scales to the spectrum. These scales were derived from the lengths of two orthogonal straight lines which pass through the center of the imaged area and terminate at the edges of the field of measurement. The resultant average spectrum is shown in Figure 7. Bearing in mind that one cannot determine the sense of motion from a spectrum on the basis of a snapshot, only two of the four quadrants contain independent information. By reviewing the video image sequence, we identified the peak of broad angular extent in the fourth quadrant with the local wind wave system and the much narrower structure in the first quadrant with the wave system generated at some distance.

The various angles required in our analysis are summarized in Figure 8. The directions of the two wave systems were estimated by eye from Figure 7. Note the close correspondence between the directions of the wind and the component of waves traveling in the $-y$ direction. Also note the near orthogonality of the local wave system and the current. Thus the current had a negligible effect on the dispersion relation for the wind-driven waves.

The estimate of $S(\omega, k_y)$ derived from an average of 16 space-time spectra is shown in Figure 9. Because the original data represent real waves, there must be symmetry through the origin in the spectrum; thus negative temporal frequencies are redundant and need not have been plotted. In the discussion below we refer only to the positive temporal frequency portion of Figure 9. However, there is a certain amount of pattern recognition necessary to interpret spectra such as these, and we think that including the redundant negative temporal frequency information aids this process. The dispersion relation given by linear theory and modified for our quasi-one-dimensional case is shown as a solid black line superimposed on the data in the upper half of Figure 9. The theoretical curve does not include a correction for wind drift, a small effect in these data since the wind speed was only 0.9 m/s and the advection from the wind drift current is only about 3% of the wind speed. The local wind waves appear at negative spatial frequencies and the waves generated at a distance at positive spatial frequencies. Both wave systems show a slight deviation from linear theory which will now be discussed.

Figure 10 presents a detailed quantitative comparison between the observations and the predictions of linear theory. The observational points were obtained by choosing a value of k_y and by scanning the space-time spectrum for that value of positive ω which corresponded to the peak in spectral density. Second-order interpolation techniques were used to refine further the estimate of this frequency. The spectrum was scanned at each harmonic of the fundamental spatial frequency out to 2 cyc/m. The fundamental spatial frequency is the inverse of the spatial baseline, 16.9 m. The data points at zero frequency and the fundamental frequency have been rejected from the analysis because they are corrupted severely by subtraction of the mean and by the Hanning weighting. Similarly, those points have been rejected for which the spectral density was more than 25 dB below the overall spectral maximum, since tests showed that the system noise caused instability in the results when the spectral density was weaker than this. The apparent phase velocity in the direction of the sampling baseline, c_y, was computed as the ratio $\omega/|k_y|$. Error bars have been assigned by attributing an error of ± 0.059 Hz to the temporal frequency estimates, which is plus or minus half the frequency resolution of this analysis.

Comparison with theory is limited mainly by our inexact knowledge of the directions of propagation of the various

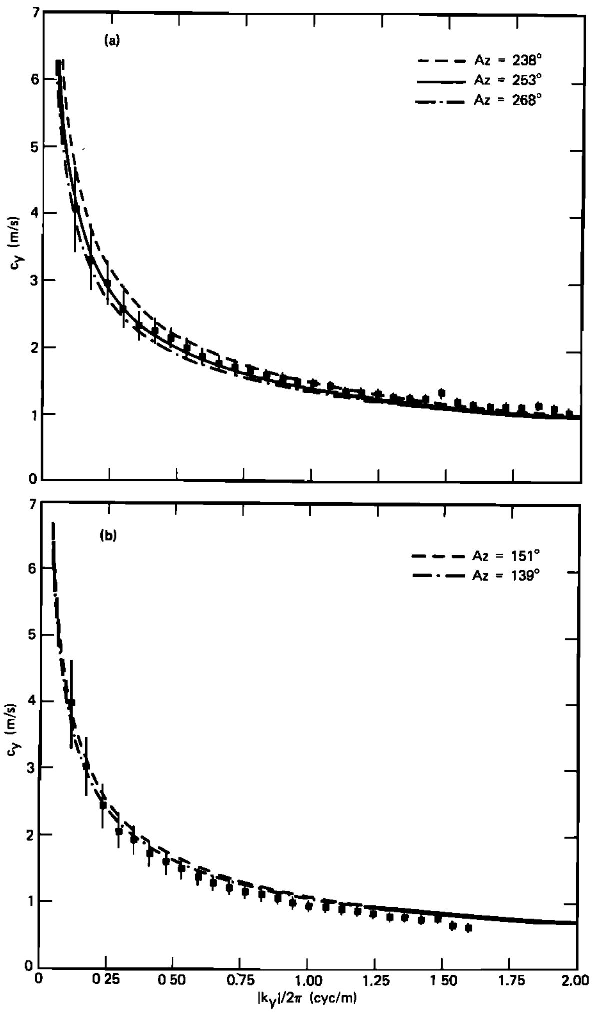

Fig. 10. Phase velocity measured along the y axis versus spatial frequency. The observational points were obtained from the space-time spectrum (see text). The smooth curves were derived from linear theory and are shown for several assumed azimuths centered on the best estimate of the wave propagation direction. (*a*) Wind-driven waves showing a slight excess phase velocity above $\simeq 1$ cyc/m. (*b*) Waves generated at a distance showing a slight deficiency in phase velocity over most of the spatial frequency range. Note that the theoretical curve corresponding to the best estimate in direction lies between the two curves shown, and it has been omitted for clarity.

wave components. Consequently, there are three theoretical curves shown in Figure 10*a*, all of which are based on linear wave theory. The middle curve corresponds to our best estimate of the propagation direction of the wind-driven waves, and the other two curves correspond to directions $\pm 15°$ about this best estimate. There is good agreement with linear theory out to $k_y/2\pi \simeq 1$ cyc/m, ($k/2\pi \simeq 1.3$) with a slight excess phase velocity at higher frequencies.

Figure 10*b* shows a similar comparison between observation and theory for the waves generated at a distance. Because of the narrowness of the two-dimensional spectrum, more accurate determination of the propagation direction of these waves can be made than for the locally generated waves. The two curves shown correspond to $\pm 6°$, about the best estimate in wave propagation direction. The best estimate itself lies between these curves but has been eliminated for clarity in the illustration. Over most of the frequency range the observations lie below the theoretical curves, implying a phase velocity less than predicted by linear theory. One possible explanation for this discrepancy is an error in the current speed used in the theoretical calculation. Although measured to be 0.25 m/s at 3 m depth, a value of 0.35 m/s would bring close agreement between theory and observation. This change in the assumed current would have a negligible effect on the locally generated wave curve since these waves propagated nearly orthogonal to the current and the wind-driven waves.

CONCLUSIONS

The technique described shows promise for remotely measuring the dynamics of waves with high resolution in space and time. It suppresses much of the error in phase speed estimates from a small number of wave gauge elements as was used by previous investigators, for which the propagation directions were inadequately resolved.

Measurements on September 27, 1978, of wind-driven gravity waves showed close agreement with linear theory up to ~1 cyc/m, but with some excess phase velocity at higher spatial frequencies. A second wave system which was simultaneously present appears to have had phase velocities which were slightly less than predicted by linear theory.

Acknowledgments. We are grateful to B. Morgan for a number of computer programs, particularly an efficient two-dimensional Fourier transform. R. Gasparovic suggested the correction of the space-time data by dividing by the normalized rms fluctuation. A. W. Bjerkaas provided data from the wave gauge array in advance of publication, and also made a number of helpful comments. A. Santos and J. Phipps designed the special modifications to our commercial CCD camera.

REFERENCES

Barber, N. F., A diffraction analysis of a photograph of the sea, *Nature, 164,* 485, 1949.

Kasevich, R. S., Directional wave spectra from daylight scattering, *J. Geophys. Res., 80,* 4535–4541, 1975.

Lake, B. M., and H. C. Yuen, A new model for nonlinear wind waves, *J. Fluid Mech., 88,* 33–62, 1978.

Plant, W. J., and J. W. Wright, Spectral decomposition of short gravity wave systems, *J. Phys. Oceanogr., 9,* 621–624, 1979.

Ramamonjiarisoa, A., and M. Coantic, Loi expérimentale de dispersion des vagues produites par le vent sur une faible longueur d'action, *C. R. Acad Sci., Ser. B, 282,* 111–114, 1976.

Ramamonjiarisoa, A., and J. P. Giovanangeli, Observations de la vitesse de propagation des vagues engendrées par le vent au large, *C. R. Acad. Sci., Ser. B, 287,* 133–136, 1978.

Rikiishi, K., A new method for measuring the directional wave spectrum, *J. Phys. Oceanogr., 8,* 508–529, 1978.

Stilwell, D., Directional energy spectra of the sea from photographs, *J. Geophys. Res., 74,* 1974–1986, 1969.

Stilwell, D., and R. O. Pilon, Directional spectra of surface waves from photographs, *J. Geophys. Res., 79,* 1277–1284, 1974.

Von Zweck, O., Observations of propagation characteristics of a wind-driven sea, Ph.D. thesis, Mass. Inst. of Technol., Cambridge, Mass., 1970.

Yefimov, V. V., Y. U. P. Solov'yev, and G. N. Kristoforov, Observational determination of the phase velocities of spectral components of wind waves, *Izv. Acad. Sci. USSR Atmos. Oceanic Phys., Engl. Transl., 8,* 246–251, 1972.

(Received October 29, 1979;
revised February 28, 1980;
accepted March 10, 1980.)